Application of Internal Standard Method in XRD Testing and Analysis

1. Background

XRD powder diffraction instruments exhibit certain systematic errors primarily, which are briefly described in Table 1. Among these errors, instrument zero point, 2θ/θ motor drive matching, counting lag, air refraction, and temperature errors can be minimized by adjusting instrument precision or external environment, but cannot be eliminated through data processing; only corrected using standard samples. For sample transparency, and axial divergence, experimental methods can be employed such as using thin-film analysis for highly transparent samples and reducing slit pitch while increasing sample length to minimize measurement errors. Among the errors listed in Table 1, zero-point errors, motor drive imperfections, counting lag, air refraction, and temperature errors can be minimized by adjusting instrument precision or external environment, but can only be eliminated using standard samples. Therefore, eliminating measurement errors first requires standard sample correction, followed by obtaining precise spectra through mathematical processing.[1,2]

The standard sample is added to the experimental sample, and the correction is performed by comparing the measured diffraction lines of the standard sample with its expected value. This method is referred to as the "internal standard method". The standard material should be selected with stable crystal cell parameters, such as single-crystal silicon (Si) and LaB_6, with a measurement range of 10-80°.

Error	Cause	Effect
Zero-point error	Any misalignment or offset in the angular zero position of the diffractometer	Systematic peak shifts
Axial divergence	X-ray beam diverges out of focusing circle plane	Asymmetric broadening of diffraction peaks, especially at low angles; peak shifts
Transparent sample	X-ray beam penetrates too deep into the sample, part of the diffraction beam is below the focusing circle	Asymmetric broadening of diffraction peaks; peak shifts
Imperfections in motor drive system	Any misalignment in motor drive system controlling angular positions of the X-ray tube and detector (gear eccentricity, radius misalignment, etc.)	Systematic peak shifts and angle dependent deviations
Counting lag	System does not fully register true peak intensity before continuing to next angular position	Distorted peak shapes, peak shifts, incorrect intensities
X-ray diffraction through air	Air absorbs and scatters a small fraction of the X-ray beam, reducing effective beam intensity	Reduced intensity and increased noise, impacts high accuracy quantitative phase analysis
Temperature variation	Small temperature variations can occur between laboratories	Thermal expansion/contraction changes crystal lattice spacing

Table 1: Common systematic errors in X-ray diffractometry

Crystallographic parameters are critical parameters of crystalline materials, which are not static. Bond energy, density, thermal expansion, solid-state phase transitions, and macroscopic stress in crystals are all closely related to these parameters. Therefore, variations in crystallographic parameters can elucidate the essence and patterns of crystal transformations. Lithium iron phosphate ($LiFePO_4$) is a widely used cathode material in batteries, and the variation of its unit cell parameters directly affects the overall battery performance.[3,4]

The transformation of amorphous carbon into graphite is a crystallization process characterized by the shift from an amorphous to a crystalline state. The degree of crystallinity is quantified by the graphitization degree (G). Silicon-carbon composites are a common anode material for graphite batteries. The degree of graphitization of silicon-carbon composite is directly related to the preparation process of the material and the performance of the whole battery.[5,6]

In this experiment, LaB_6 was employed as the internal standard to precisely measure unit cell parameters for $LiFe(PO_4)$ and the graphitization of silicon-carbon composite.[7,8]

2. Experiment

The **AMI Lattice Pro X-ray diffractometer** was used for all measurements, and the experiment parameters are described in Table 2. The standard LaB_6 material (99.9%) was ground in an agate mortar, sieved through a 350-mesh standard sieve, and then heated under vacuum at 1000°C for 1 hour. For lithium iron phosphate analysis, 0.6 g of the pretreated LaB_6 and 2.4 g of the lithium iron phosphate sample were thoroughly mixed in the mortar, followed by flat plate sample preparation. For silicon-carbon composite analysis, 0.23 g of the pretreated LaB_6 was thoroughly mixed with 0.77 g of silicon-carbon in the mortar, followed by flat plate sample preparation.

Parameter	Value
Radiation Source	Cu Kα(λ=0.15406 nm)
Tube Voltage/Current	40 kV/20 mA
Scanning Mode	θ/θ Continuous Scanning
Divergence Slit	0.2 mm
Step Size/Scanning Speed	0.018°, 3°/minute
Scanning Angle Range	10°-80° (2θ)

Table 2: Experimental parameters for internal standard XRD measurements

3. Results

3.1 Unit cell parameters of lithium iron phosphate

The XRD spectra of the mixture are shown in Figure 1a. Through phase analysis, only two phases, $LiFe(PO_4)$ and LaB_6, were identified in the sample mixture. By fitting all diffraction peaks in the XRD spectra, the 2θ angles of each peak were determined. LaB_6 was then selected as the angle correction parameter. As clearly demonstrated in Figures 1(b-d), the corrected diffraction peaks exhibited slight shifts (toward lower angles) compared to the original spectra. Re-fitting the corrected XRD spectra yielded the crystal cell parameters of lithium iron phosphate (see Figure 2). Lithium iron phosphate belongs to the orthorhombic crystal system with the space group Pnma (62). The unit cell parameters

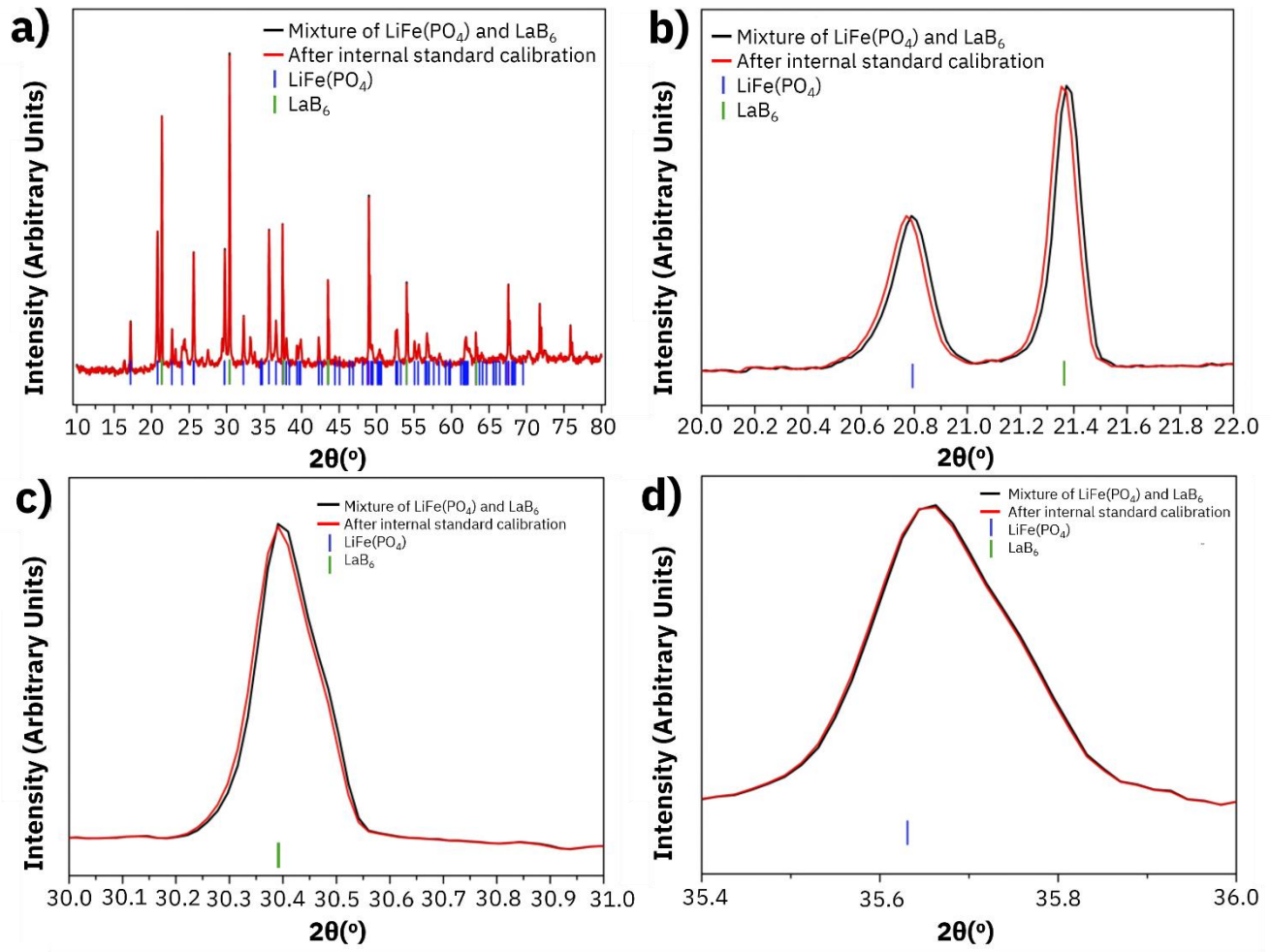

Figure 1: XRD spectra of lithium iron phosphate ($LiFePO_4$) corrected with internal standard LaB_6

	***a* (Å)**	***b* (Å)**	***c* (Å)**
Before correction	10.32	6.002	4.6885
After correction	10.31611	5.9804063	4.701392

Table 3: Calculated lattice parameters of $LiFe(PO_4)$ before and after internal standard correction

before and after refinement are shown in Table 3. These results indicate small errors in crystal cell parameters without the use of internal standard correction. Without this correction, errors in 2θ angles would lead to incorrect trends in parameter variations. Internal standard correction not only enhances the absolute accuracy of crystal cell parameters but also ensures comparability and reliability of parameter trends across different batches of samples.

3.2 Silicon carbide crystallization and graphitization

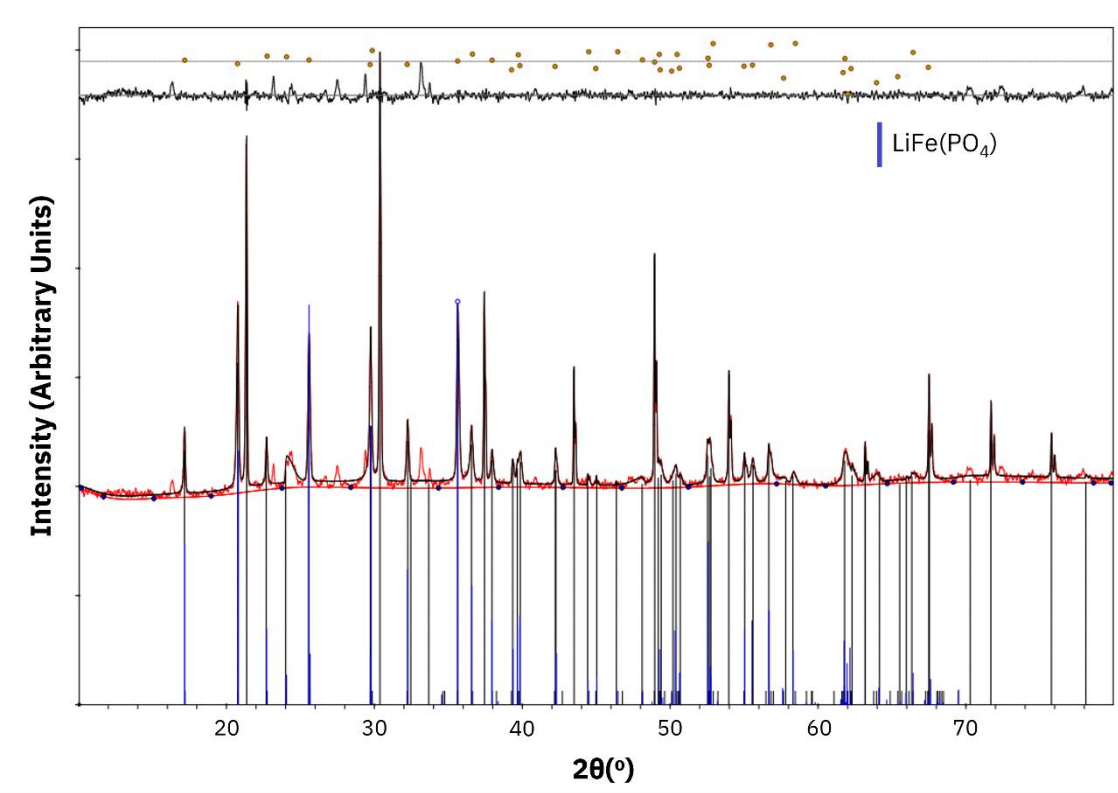

Figure 2: Full-fit XRD spectra of $LiFe(PO_4)$ after internal standard calibration

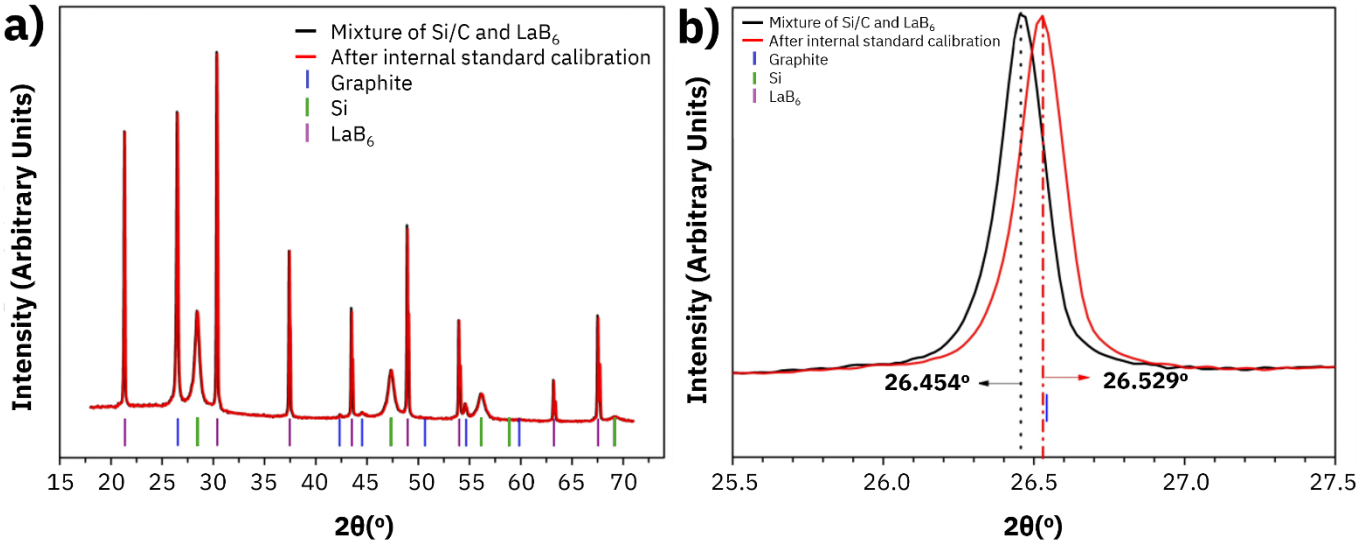

Figure 3: a) Full XRD spectra corrected with the silicon-carbon internal standard LaB_6 and b) zoomed in on (002) graphite peak

The XRD spectra of the silicon-carbon anode mixed with the internal standard are shown in Figure 3a. Through phase analysis, it was confirmed that the mixed sample contains not only graphite and LaB_6 phases but also silicon phases. By fitting all diffraction peaks in the XRD spectra, the 2θ angles of each peak were determined. LaB_6 was selected as the angle correction parameter. As clearly observed in Figure 3b, compared to the original spectra, the corrected diffraction peak positions

	2θ (°)	Crystal plane spacing, d (nm)	Degree of graphitization (%)
Before correction	26.464	0.33665	87.79
After correction	26.529	0.33572	96.26

Table 4: Diffraction peak positions for (002) graphite peak, d-spacing, and degree of graphitization calculated for silicon-carbon composite before and after internal standard correction

exhibited a shift towards higher angles. Comparing the positions of the main (002) crystal plane diffraction peak before and after correction (Table 4), the uncorrected value was 2θ=26.454°, corresponding to a crystal plane spacing of d=0.33665nm and a G value of 87.79%. After angle correction, the corrected 2θ value became 26.529°, with the crystal plane spacing reduced to 0.33572nm, yielding a G value of 96.28%. The graphitization degree results indicate that the corrected G value increased, demonstrating improved accuracy. This enhancement corresponds to the sharp and symmetric appearance of the main (002) crystal plane diffraction peak in the XRD spectra.

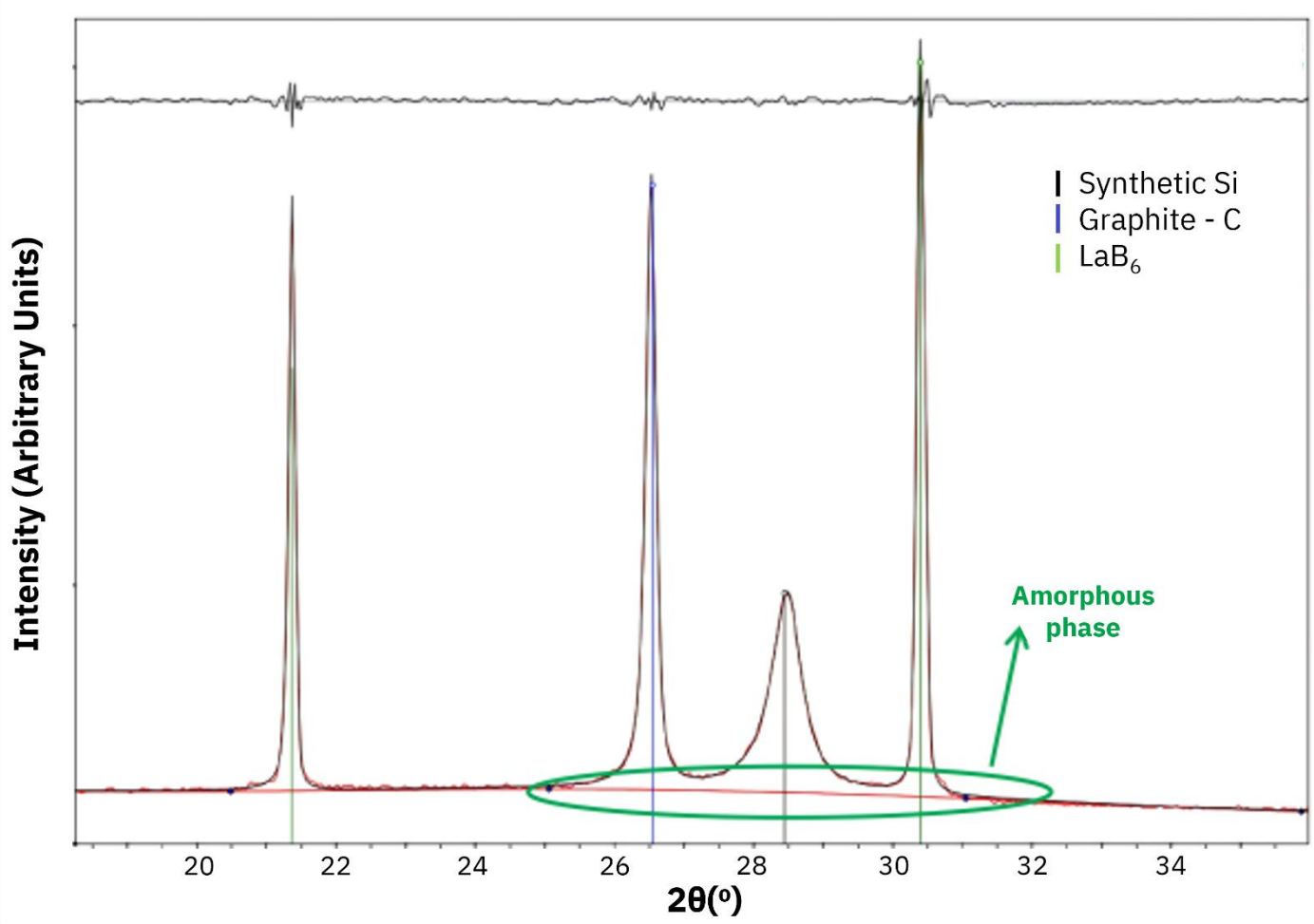

Figure 5: Partial XRD spectra of silicon-carbon after calibration with internal standard LaB_6

The XRD spectra of the silicon-carbon composite mixed with the internal standard are shown in Figure 5. Through phase analysis, it was confirmed that the mixed sample contains not only graphite, silicon, and LaB_6 phases but also a certain amount of amorphous material. The analysis revealed a silicon-carbon graphitization degree of 96.28%, indicating incomplete crystallization of the sample. After full fitting of the XRD spectra, local diffraction peaks were selected for analysis as shown in Figure 5 to determine the areas of different phases.

Species	Calculated weight percent (%)		
	Corrected, with LaB_6 mass	Corrected, LaB_6 mass subtracted	Expected composition
Si	33.5	43.5	43.5
Graphite	36.7	47.6	47.7
Amorphous	6.8	8.9	8.8
LaB_6	23.0	-	-

Table 5: Phase composition analysis of silicon-carbon composite after internal standard correction compared with expected values

Quantitative analysis yielded the mass fractions of various phases, shown in Table 5. With the mass of LaB_6 removed, the weight percentages of each phase closely align with the expected phase composition of the original silicon-carbon sample for Si (43.5%), graphite (47.6%), and amorphous phase (8.8%).

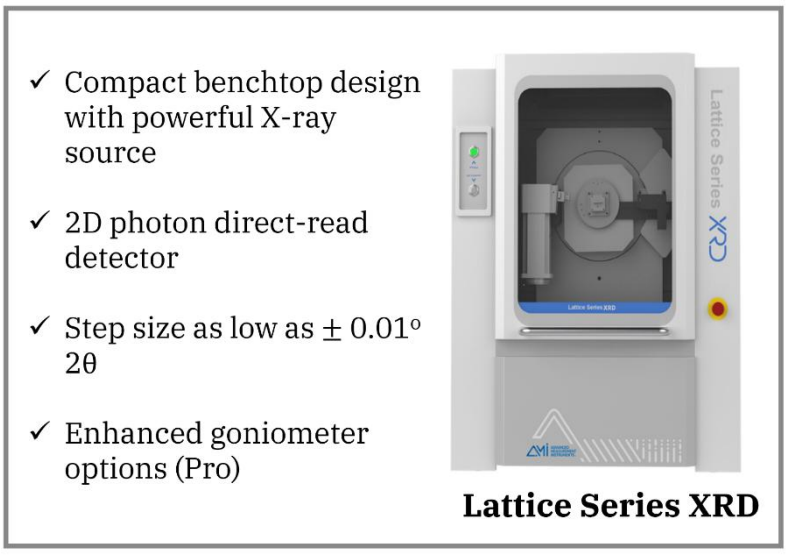

*Figure 6: Highlighted features of **Lattice Series XRD** from **AMI***

4. Conclusions

This application note shows that the LaB_6 standard material can be added to the sample to eliminate systematic instrument error and the off-axis error of the sample plate. Then, the XRD spectrum can be measured by the internal standard method and the crystal cell parameters, graphitization, and quantitative phase analysis of the material can be determined accurately and reproducibly. The **Lattice Series XRD** from **AMI**, shown in Figure 6, combines high-power performance with a compact, benchtop design with the high precision required for internal standard calibration. All models offer excellent signal to noise ratio and fast scan speeds, resulting in improved data quality ideal for calibration.

5. References

(1) Wu, P. J.; Yao, C. Y.; Cao, L. Y.; Huang, J. F.; He, H. Y.; Zhu, H. Foundation of the standard curve database for the quantitative analysis by internal standard method based on XRD. *Adv. Mater. Res.* **2010**, *177*, 1-4.
(2) Zhao, P.; Lu, L.; Liu, X.; De la Torre, A. G.; Cheng, X. Error analysis and correction for quantitative phase analysis based on Rietveld-internal standard method: Whether the minor phases can be ignored? *Crystals*, **2018**, *8*, 110.
(3) Hadouchi, M.; Koketsu, T.; Hu, Z.; Ma, J. The origin of fast-charging lithium iron phosphate for batteries. *Battery Energy*, **2022**, *1*, 20210010.
(4) Wang, G. X.; Needham, S.; Yao, J.; Wang, J. Z.; Liu, R. S.; Liu, H. K. A study on $LiFePO_4$ and its doped derivatives as cathode materials for lithium-iron batteries. *J. Power Sources*, **2006**, *159*, 282-286.
(5) An, Y.; Tian, Y.; Wei H.; Xi, B.; Xiong, S.; Feng, J.; Qian, Y. Porosity- and graphitization-controlled fabrication of nanoporous silicon@carbon for lithium storage and its conjugation with MXene for lithium-metal anode. *Adv. Func. Mater.* **2019**, *30*, 1908721,
(6) Huang, S.; Guo, H.; Li, X.; Wang, Z.; Gan, L.; Wang, J.; Xiao, W. Carbonization and graphitization of pitch applied for anode materials of high power lithium ion batteries. *J. Solid State Electrochem.* **2013**, *17*, 1401-1408.
(7) Ning, G. and Flemming, R. L. Rietveld refinement of LaB_6: Data from μXRD. *J. Appl. Cryst*. **2005**, *38,* 757-759.
(8) Black, D. R.; Mendenhall, M. H.; Brown, C. M.; Henins, A.; Filliben, J.; Cline, J. P. Certification of standard reference material 660c for powder diffraction. *Powder Diffraction*, **2020**, *35*, 17-22.